Electron-hole plasma formation dynamics observed through exciton-plasma interactions in transition metal dichalcogenides

Manobina Karmakar, Subhrajit Mukherjee,[*] Samit K. Ray, and Prasanta Kumar Datta[†]

Department of Physics, Indian Institute of Technology Kharagpur, Kharagpur 721302, India

How do the many-particle interactions evolve in semiconductors is crucial for understanding light-matter interactions. We observe Coulomb-correlated electron-hole plasma formation via its interaction with excitons in a transition metal dichalcogenide semiconductor. We observe that under intense photoexcitation $\sim 10^{19}$ per cm^3, huge damping destroys the Coulomb correlation and hinders the plasma formation until a majority of the free carriers recombine and the plasma oscillation period becomes sufficiently smaller than the damping time constant. Moreover, only 1%–3% of the injected free carriers form Coulomb-correlated plasma. Our study sheds light on exciton-plasma interactions and quasistatic Coulomb screening, which play pivotal roles in device engineering.

I. INTRODUCTION

Coulomb-correlated electron-hole plasma (EHP) formation is one of the most intriguing phenomena in the context of light-matter interaction, many-particle phenomena, and semiconductor device physics. EHP is a dressed many-particle state, where negatively charged electrons form a screening cloud around positively charged holes and vice versa. This leads to local density fluctuations that propagate through longitudinal waves with a frequency known as plasma frequency (ω_{pl}), provided the oscillation periods are sufficiently smaller than the dominant damping time constant τ ($\omega_{\mathrm{pl}}\tau \gg 1$) [1]. The presence of free carriers and EHP drastically modify semiconductor optical properties, especially those possessing strongly bound electron-hole pairs or excitons. Tunability of excitonic properties are mostly achieved by altering EHP density in the material [2–6]. As the uncorrelated charge carriers transform to a Coulomb-correlated EHP, they screen quasistatic Coulomb interactions leading to quasiparticle band gap renormalization (BGR) [6–10]. Device realization in a wide range of optoelectronic applications requires external charge carrier injection [3,11–15], where correlated EHP formation plays a crucial role in tuning optical properties. Chernikov *et al.* have observed a broad range of tuning in exciton binding energy via controlling the free-carrier density in a monolayer WS$_2$ based field-effect transistor device. Since bound and free electron-holes coexist in such semiconductors, excitonic devices [15] are sensitive to the extent of the coexisting correlated plasma.

The transition from a free-carrier gas to a correlated EHP is not instantaneous. Huber *et al.* have demonstrated that plasma formation is retarded by a timescale related to the inverse of the plasma frequency [16]. Nevertheless, this time-resolved study was performed for a specific excitation density (2×10^{18} per cm^3) in GaAs. It is not clear whether the entire free-carrier gas converts to Coulomb-correlated plasma in all semiconductors, irrespective of the input carrier density magnitude. Recently, Steinhoff *et al.* have theoretically calculated the fraction of EHP for a range of carrier injection densities in excitonic semiconductors, namely transition metal dichalcogenides [17] in thermal equilibrium. However, the experimental distinction between carrier and EHP and the transition of the former to the latter remains unexplored in a wider context.

Probing carrier-induced dynamics of excitonic states is advantageous to observe free-carrier gas to EHP transition, as Coulomb screening renormalizes band gap upon EHP formation, whereas state-filling effects introduce exciton bleaching, which originates from the individual fermionic nature of the charge carrier and is independent of the Coulomb correlations. Despite this advantage, the superposition of excitonic, free-carrier, phonon, and EHP-induced dynamical effects in the time-resolved optical experiments renders the problem much involved [6,18–21]. Possibly, this is the prime reason why uncorrelated carriers and EHPs have not been individually recognized in semiconductors. In the present study we choose a transition metal dichalcogenide material (TMDC) MoS$_2$ that possesses strongly bound excitons even at room temperature. We use broadband transient absorption (TA) spectroscopy to carefully monitor the time evolution of the *C* exciton oscillator strength and resonance energy upon carrier injection. We perform TA experiments at different pump-photon energies, pump fluence (i.e., input carrier densities), as well as different sample environments, and analyze the data to isolate phonon, carrier, and exciton-induced dynamical processes systematically. Especially, we identify second-order kinetics of the electron-hole recombination process, unlike exciton recombination and carrier-phonon coupling that follow first-order kinetics. We observe that in the presence of intense photoexcitation of order 10^{19} per cm^3, huge damping, possibly originating from carrier-carrier scattering, slows down the

---

[*]Present address: Faculty of Materials Science & Engineering, Technion Israel Institute of Technology, Haifa 3203003, Israel.
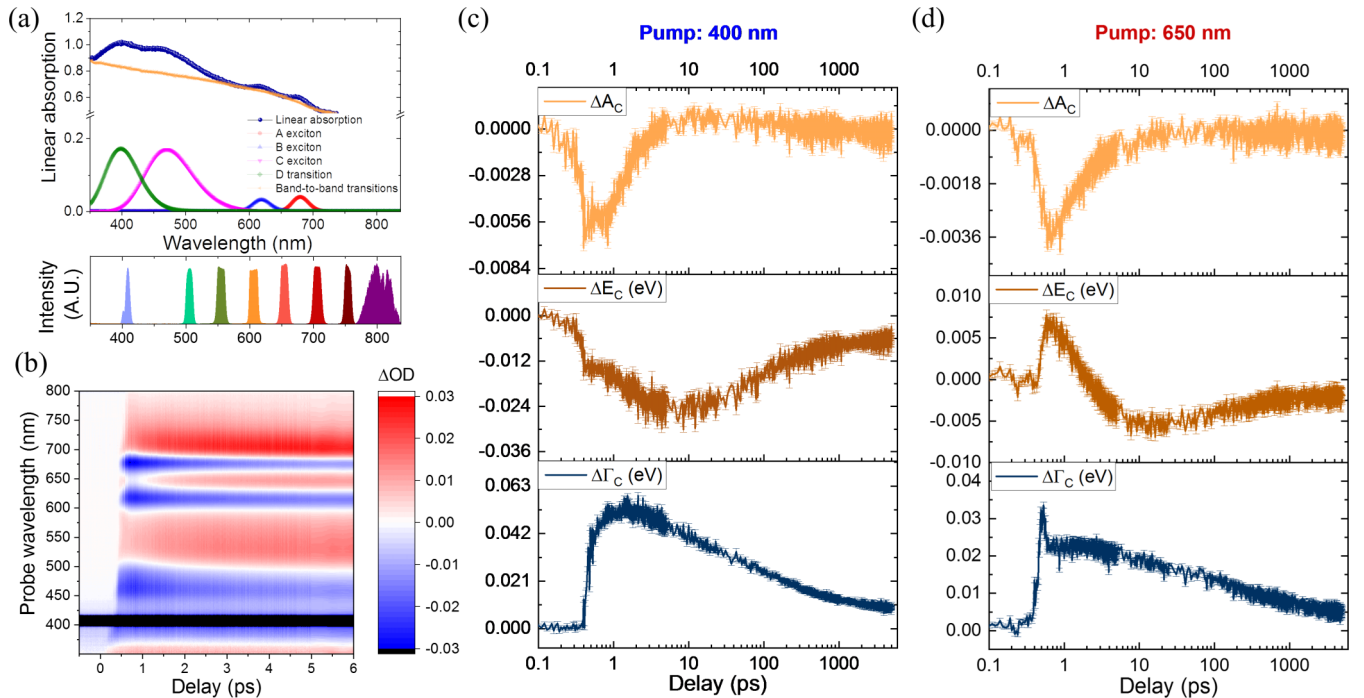
[†]pkdatta@phy.iitkgp.ac.in

075446-1

FIG. 1. (a) (Upper panel) Linear absorption spectrum (extinction coefficient times sample length αl) of multilayered MoS_2 obtained by an ultrafast supercontinuum pulse. Corresponding A, B, C, and D excitonic line shapes are disentangled from the continuous background of the band-to-band absorption spectrum and are depicted in the same scale (note the break in the absorption axis). (Lower panel) The optical spectrum of the various pump excitations utilized in this work. The peak amplitudes of the same are in arbitrary units. (b) Transient absorption spectra for 400 nm pump excitation at probe wavelength 375 to 800 nm. Temporal evolution of oscillator strength, resonance energy, and linewidth of C exciton in the presence of (c) 400 nm and (d) 650 nm pump excitation.

plasma formation up to ~8 ps. Meanwhile, most free carriers recombine, and only a small fraction (1%–3%) of the optically injected carriers form the dressed plasma states.

II. RESULTS AND DISCUSSIONS

Multilayered MoS_2 sample on a thin quartz substrate is prepared through sono-chemical exfoliation [22] of bulk MoS_2 (see Ref. [23], Sec. S1 for further details). The atomic force microscopy data reveals an average sample thickness of 30 nm with a standard deviation of 20 nm (see Fig. 1 in Ref. [23]). Precisely, flake thicknesses ranging from 15 to 40 nm have the highest probability and therefore dominates the optical response. Sample inhomogeneity does not play any significant role in the transient absorption data in the studied timescale in the context of heat and carrier diffusion due to low interlayer diffusion coefficients [24–27]. An elaborate discussion can be found in Sec. S2.1 of Ref. [23], which includes other relevant references [28–34].

Here we use a multilayered film instead of a monolayered TMDC as we intend to explore Coulomb screening effects on excitons. Environmental screening from quasiparticles and dielectric screening is efficient while sample thickness is considerably higher compared to the characteristic lengths of the excitation, here excitonic Bohr radius (approximately a few nanometers in TMDCs [35,36]).

Figure 1(a) describes the linear absorption [$A(\lambda)$] spectrum of the multilayered MoS_2 obtained by a broadband supercontinuum pulse. Conventional A, B, C, and D excitonic

transitions centered around 674, 615, 470, and 400 nm, respectively, are disentangled from the continuous absorption background of band-to-band transitions by obtaining a second derivative [37] and are indicated therein (see Ref. [23], Sec. S5.1 for more details). We measure transient absorption due to intense, ultrafast optical excitation (pump) of various wavelengths (λ_p: 400 and 500 to 800 nm having an interval of 50 nm) and especially examine the C excitonic properties induced by the carriers and plasma up to ~6 ns. Further details of our setup [37–39] is presented in Sec. S2 of Ref. [23]. As multilayered MoS_2 has an indirect band gap at 1.29 eV [40], each pump-photon energy enables free-carrier generation. Parallel valence and conduction bands (band nesting) at several k points of TMDCs lead to high optical conductivity constituting broad and intense C exciton transition [41]. This exciton, as compared with band edge A and B excitons, has higher binding energy, oscillator strength, and Mott density, and therefore allows us to explore a broad range of exciton-carrier interaction dynamics without being saturated and ionized. We are interested in studying exciton-free carrier interactions where pump excitation creates free carriers. A resonant probe tuned to an excitonic state measures the temporal evolution of the exciton-plasma (or free carrier) interactions. Here we choose the C excitons whose energy is higher than most of the pump-photon energy used in the experiment. This prevents the formation of pump-generated C excitons in below-resonance excitation conditions and facilitates distinguished observation of exciton-carrier (or plasma) interactions. Additionally, lack

of understanding of this band-nesting exciton dynamics has influenced us to choose this particular state for studying exciton-plasma interactions. Here, pump-induced C exciton formation is limited to 400 and 500 nm excitation, whereas higher wavelengths energetically forbid the formation of the C exciton. The spectra of the chosen pump pulses are displayed in Fig. 1(a), lower panel; peak intensities are in arbitrary units.

We use pump fluence (F) of order 10 μJ/cm^2 and maintain $FA(\lambda)$ to a constant value that ensures initial carrier density 10^{19} per cm^3 (see Ref. [23], Sec. S4). To ensure that we photoexcite the material in the linear (single-photon) absorption regime, we verify the linearity of the differential absorption (ΔOD) with pump fluence and observe linear variations for all pump wavelengths in the mentioned fluence range except that of 750 nm (see Ref. [23], Sec. S3). In the case of the 750 nm pump wavelength that enables two-photon absorption, we increase the fluence by one order to obtain ΔOD values comparable to that of the other pump wavelengths. We depict a pseudocolor representation of the ΔOD spectrum ($\lambda_p = 400$ nm) as a function of probe delay and probe wavelength in Fig. 1(b). The ΔOD spectrum in the 400 to 570 nm probe region originates from the pump-induced alterations of the C and D excitonic properties. We model the differential absorption spectrum in the mentioned probe wavelength range to disentangle the pump-induced evolution of oscillator strength (ΔA_C), resonance energy (ΔE_C), and linewidth ($\Delta \Gamma_C$) of C exciton (see Ref. [23], Sec. S5). We repeat this for the whole range of probe delays for each pump wavelength to obtain the excitonic parameters' dynamical evolution. Figures 1(c) and 1(d) plot the temporal evolution of these excitonic properties upon 400 and 650 nm pump excitation, respectively. We note that photoinduced oscillator strength (OS) of C excitons reduces by 5%–10% following ultrafast excitation, irrespective of the pump-photon energies. On the other hand, oscillator strengths of the band edge (A and B) excitons drop around 60% (see Ref. [23], Sec. S9) for all pump wavelengths, except 600 nm. Notably, 600 nm excitation is ∼50 meV blue detuned with respect to the B exciton resonance. Interestingly enough, this photoexcitation triggers a Mott transition and a population inversion [42] of the B transition. This will be discussed elsewhere. However, all other transient measurements are obtained well below the Mott transition threshold of A, B, C, and D excitons. Moreover, the C exciton dynamical features upon 600 nm excitation remain similar to other below-resonance excitation conditions, which do not induce any Mott transition. In the next few paragraphs we discuss the individual photoinduced dynamics of these excitonic properties, especially excitonic oscillator strength reduction and redshift, in the context of free-carrier and plasma effects. Now onward, by the word "excitons," we usually mean the C excitons, unless otherwise mentioned.

A. State-filling effects upon below-resonance pump excitation

We observe a pulsewidth-limited reduction of exciton oscillator strength (i.e., ΔA_C drops to a minimum within the instrumental response function or IRF) that reverts to zero within a few picoseconds for each λ_p. Absorption probability of an exciton state drops due to the state-filling effects orig-

inating from any of the following: (1) and (2) pump-induced electrons and holes occupy conduction band, valence band, respectively, of the band-nesting (BN) region, and (3) excitons are formed [7,43,44]. This indicates that apart from pump-induced excitons, free carriers either in the valence band or in the conduction band can induce state filling of the exciton. As the pump-induced quasiparticles recombine through different channels, the bleaching effect reverses following similar dynamics. Exciton recombination follows first-order kinetics, whereas electron-hole recombination is a bimolecular type (second order) [45]. In case the dominant decay mechanism follows first- (second-) order kinetics, the solution of carrier density hence, bleaching is exponential (inverse linear) with respect to time delay. Here we present the ΔA_C along with the ΔA_C^{-1} for 400 and 600 nm pump excitation in Figs. 2(a) and 2(b). The inverse function varying exponentially (linearly) with time delay identifies the first- (second-) order relaxation process for 400 nm (650 nm) pump excitation. Further investigation of ΔA_C^{-1} for all other pump wavelengths confirms dominant first-order and second-order decay processes for above- and below-resonance conditions, respectively.

We model the temporal evolution of ΔA_C to obtain the recombination rate constants:

$$\Delta A_C = -\alpha_A N, \quad \frac{dN}{dt} = -k_1 N - k_2 N^2, \quad (1)$$

where $N = N(t)$ is carrier (or exciton, as applicable) density, α_A is a proportionality constant, and k_1 and k_2 are first- and second-order rate constants ($k_1, k_2 \geqslant 0$). Normalized ΔA_C can be expressed as follows:

$$\frac{\Delta A_C}{|\Delta A_C|_{\max}} = \frac{N(t)}{N_0}$$
$$= e^{-k_1 t}; \quad \lambda_p \in (400, 500 \text{ nm})$$
$$= \frac{k_1 e^{-k_1 t}}{k_1 - (e^{-k_1 t} - 1)k_2 N_0}; \quad \lambda_p \in (550, 750 \text{ nm}).$$
$$(2)$$

Excellent fitting of the data with Eq. (2) is depicted in Fig. 5 of Ref. [23]. We display obtained k_1 values as a function of λ_p in Fig. 2(c). We note that on average k_1 values are ∼0.9 and ∼0.1 ps^{-1} for above- and below-resonance excitation, respectively. For 400 and 500 nm pump excitation, pump-induced C exciton population leads to state filling in probe resonance. Therefore, we attribute ∼0.9 ps^{-1} rate constant to direct exciton recombination. As free carriers dominate the bleaching dynamics for 550 to 750 nm pump, we attribute ∼0.1 ps^{-1} monomolecular rate constant to the defect-assisted hole and electron capture. Similar values of capture rates have been reported previously [46]. We identify k_2 as the electron-hole recombination rate [$\lambda_p \in (550, 750)$ nm]. We rule out exciton-exciton annihilation that too follows a second-order kinetics [19], as exciton formation remains prohibited in this case. We find that the product of electron-hole recombination rate constant and the initial carrier density that induces state filling (leading to exciton bleaching), that is, $k_2 N_0$ is independent of the pump-photon energy. The $k_2 N_0$ values are depicted as a function of λ_p in Fig. 3(f). The values are
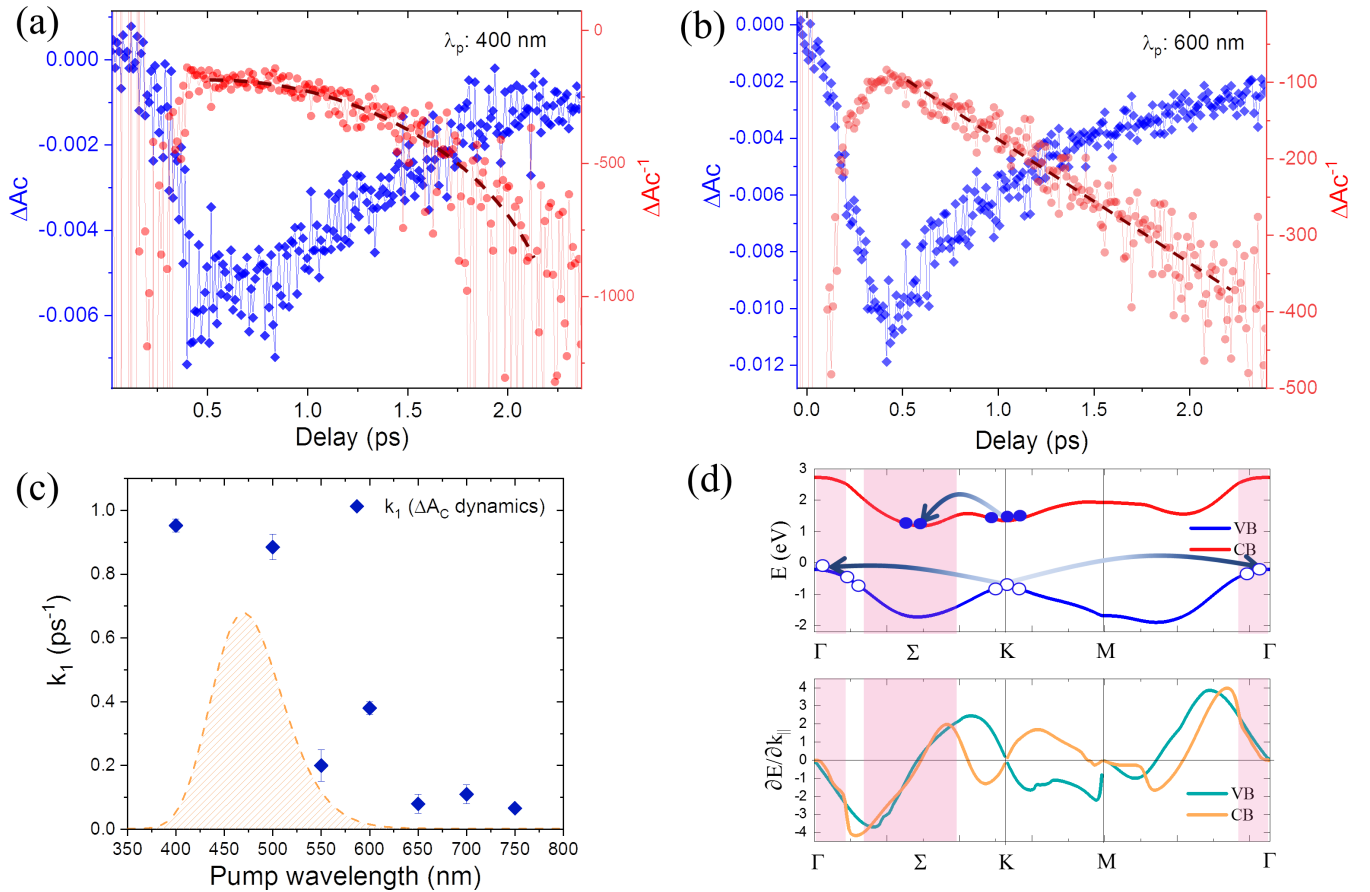
FIG. 2. Temporal evolution of ΔA_C and the corresponding ΔA_C^{-1} for (a) 400 nm (above-resonance) pump and (b) 600 nm (below-resonance) pump excitation. We add dashed lines of exponential and linear types on the ΔA_C^{-1} as a guide to the eye. (c) The first-order rate constant at different pump wavelengths as estimated from the model in Eq. (2). The spectral shape of the C exciton is indicated by dashed lines in arbitrary units for reference. (d) (Upper panel) Valence band maxima and conduction band minima of multilayered MoS$_2$ adapted from Ref. [37]. (Lower panel) Gradient of the valence band maxima and conduction band minima are displayed. Same values (within 1 eV/$\frac{2\pi}{a}$, where a is the in-plane lattice constant) of the gradients indicate maxima in the joint-density-of-states that correspond to the C exciton states. Filled and unfilled circles indicate photoinduced electrons and holes. Intervalley scattering paths are depicted by arrows.

around 1 ps^{-1}. Inserting N_0 value as the initial carrier density (10^{19} per cm^3), we estimate the electron-hole recombination rate $k_2 = 10^{-7}$ cm^3 s^{-1}, very similar to an earlier report in MoS$_2$ monolayer [45]. One must note that N_0 values are less than the corresponding excitation densities since a part of the photoexcited coherent excitations form excitons. Therefore, this value provides only an estimate on the lowest possible value of k_2.

To depict the pathways for exciton bleaching in the presence of different pump energies, including below-resonance energy, we plot valence band and conduction band extrema along with respective gradients in parallel k direction ($\frac{\partial E}{\partial k_{\parallel}}$) in Fig. 2(d). This data are adapted from the band structure of multilayered MoS$_2$ from an earlier work [37]. The highlighted red portions display the k points related to the BN region possessing a quasiparticle band gap of 2.94 eV. The transition metal dichalcogenides possess an involved energy-momentum landscape where intervalley scattering plays an important role in the population of different valleys. In the schematic band structure of MoS$_2$ in Fig. 2(d), we indicate energetically favorable intervalley scattering pathways that can create state-filling effects for the C excitons (in the probe),

even when the pump-photon energy is less than the particular excitonic state, and no excitons are formed. We note, as long as the pump-photon energy is sufficient to induce transitions at the K point, yet is insufficient to directly excite the BN region, intervalley scattering allows either electron or holes in the BN region [pathways are shown by curved arrows in Fig. 2(d)]. Especially, Σ being the global minima of the conduction band, the majority of photoinduced carriers scatter to this valley associated with the BN. Recent time-resolved photoemission spectroscopy experiments have revealed strong $K \rightarrow \Sigma$ scattering within 100 fs in bulk TMDCs [47–49] that justifies the IRF-limited observation of exciton bleaching due to intervalley scattering following below-exciton resonance excitation (i.e., 550 to 750 nm pump).

B. Band gap renormalization dynamics and electron-hole plasma to free-carrier ratio

Excitonic bleaching is related explicitly to the individual fermionic nature of charge carriers, that is, Pauli exclusion principle, and is independent of Coulomb correlations. On the other hand, exciton resonance energy
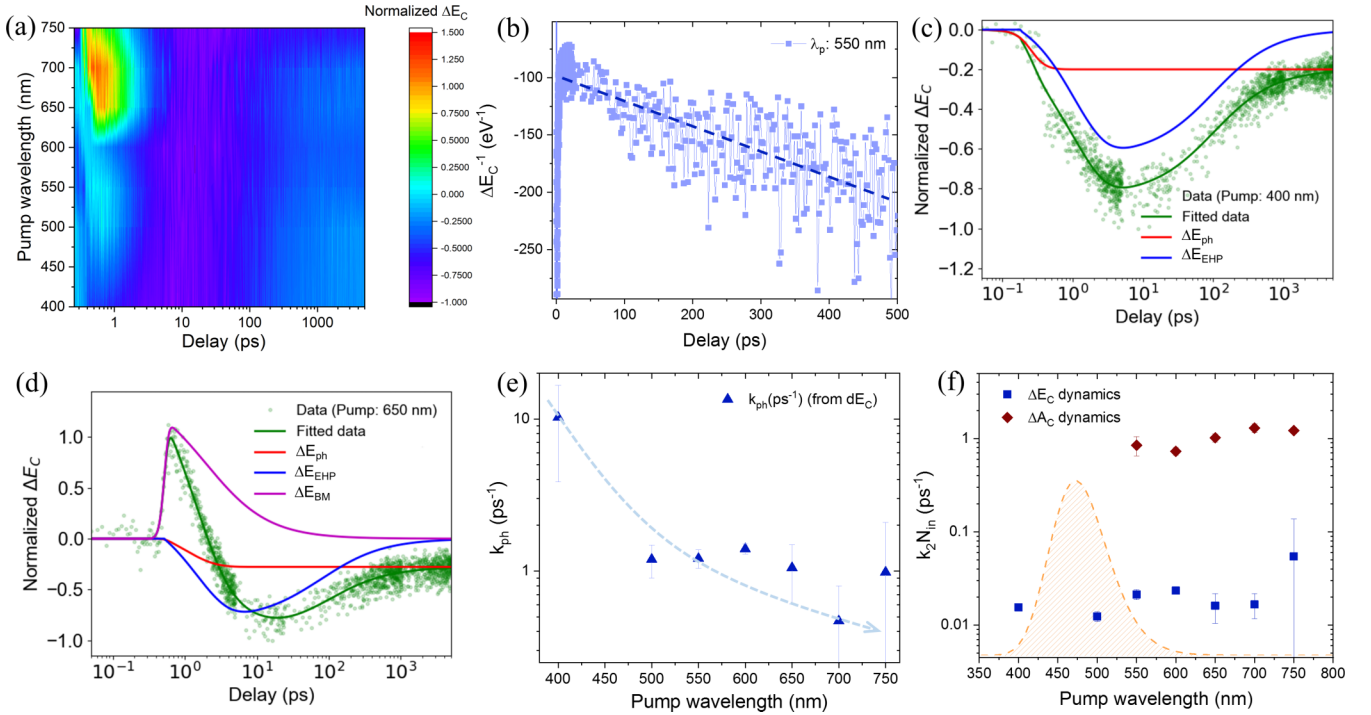
FIG. 3. (a) Pump-induced alteration of C exciton resonance energy (normalized ΔE_C) as a function of pump wavelength and probe delay. (b) Linear variation of ΔE_C^{-1} with delay for $\lambda_p = 550$ nm. (c) Time evolution of ΔE_C and the corresponding contributions from the phonon-induced lattice heating (ΔE_{ph}) and electron-hole plasma screening (ΔE_{EHP}) for $\lambda_p = 400$ nm. (d) Similar variations for $\lambda_p = 650$ nm which also includes an initial blueshift component due to exciton binding energy reduction (ΔE_{BE}). (e) Phonon rate constants that indicate hot-carrier cooling timescale. (f) Comparison of the second-order rate constant times initial carrier density as obtained from fitting the bleaching and resonance energy renormalization dynamics with Eq. (2) and Eqs. (4) and (5), respectively. The C exciton absorption spectrum is depicted (arbitrary units in y axis) in dashed lines for convenience.

($E_{exc} = E_g - E_{BE}$), which is the difference of quasiparticle band gap (E_g) and the exciton binding energy (E_{BE}), is dictated by EHP-induced band gap renormalization (BGR) (see Ref. [23], Sec. S6 for detailed discussions). Coulomb potential of an isolated charge, placed in an electron-hole plasma, is weakened (screened) through the surrounding cloud of oppositely charged quasiparticles (Coulomb hole). Moreover, the probability of two similarly charged fermions coming close to each other reduces, which in turn reduces the repulsive Coulomb interaction (exchange hole). As a result of Coulomb and screened exchange interaction, the energies of electrons and holes in their respective bands reduce introducing a redshift (δE_g) in the excitonic resonance [7,50]:

$$\delta E_g = \sum_{q \neq 0} [V_s(q) - V(q)]$$
$$- \sum_{q \neq 0} V_s(q)[f_e(q, n, T) + f_h(q, n, T)], \quad (3)$$

where $V_s(q)$, $V(q)$, $f_e(q, n, T)$, and $f_h(q, n, T)$ are, respectively, the screened and unscreened Coulomb potential in momentum space, electron, and hole Fermi-Dirac distribution function. First and second term denotes Coulomb hole and screened exchange effect (exchange hole), respectively. Another origin of quasiparticle band gap reduction is lattice heating through carrier-phonon coupling. Photoexcited hot

carriers and excitons cool down by transferring the excess energy to the phonon system, eventually leading to lattice heating [20,51]. There are several reports on subpicosecond to picosecond order carrier-phonon coupling times in transition metal dichalcogenides [20,52,53]. Moreover, Lin *et al.* have performed ultrafast electron diffraction on bi-layered MoSe$_2$ to directly observe subpicosecond to 1 ps conversion of photoenergy to lattice heating and have corroborated the experimental results with first-principles nonadiabatic quantum dynamic simulations [54].

Note that, conventionally, band gap renormalization refers to EHP-induced band gap reduction and not the lattice heating effects. The weakening of Coulomb attractive potential often leads to reduced E_{BE}, which is reflected as a blueshift of the exciton resonance. However, Coulomb potential of excitonic constituents are effectively modulated by dynamic screening, where the quasistatic EHP screening is less effective [37,55,56].

From Figs. 1(c) and 1(d) we identify that C excitons undergo a predominant redshift ($\Delta E_C < 0$) irrespective of the pump wavelength. It has a slow rise of the redshift feature that reaches a maximum ~8 ps and reverts to an offset within a few-hundred ps, as evident from the plots. The reversion within hundreds of ps (process 1) and the offset up to 5 ns (process 2) delay suggests two distinct features dictate the temporal evolution of the C exciton resonance. The decay of the latter process is beyond the temporal window of our

experiment, and hence, we obtain a nonvarying redshift. Comparing the $\Delta E_C(t = 8 \text{ ps})$ and $\Delta E_C(t = 5 \text{ ns})$, we estimate that the relative weight of processes 1 and 2 are 68% and 32%, respectively, for a 400 nm pump. We observe that the relative weight of process 1 is greater than that of process 2 for each pump wavelength ranging from 400 to 700 nm (see Fig. 8 of Ref. [23]). For 750 nm, relative weights are nearly equal, and that for 800 nm, process 2 dominates. A closer look into the initial rise of the redshift following 400 nm excitation suggests a fast rise up to 12 meV within 0.2 ps, accompanied by a much slower (few ps) rise reaching maxima up to $\sim$24 meV. It is evident that the slower rise is followed by the reversion and is associated with higher relative weight and is therefore, related to process 1. This is true for other pump wavelengths up to 700 nm as well. As discussed earlier, two possible phenomenon- EHP-induced band gap renormalization and lattice heating are responsible for the redshift of a quasiparticle band gap. Here we attribute process 1 to band gap renormalization and process 2 to phonon-induced lattice heating. The screening effect builds up until $\sim$8 ps and reduces within a few hundred ps. On the contrary, the lattice heating maximizes in a few ps, and the lattice does not cool within the experimental time window; thus, giving rise to a residual redshift. We provide an elaborate discussion on these attributions in the following paragraphs.

To understand the decay mechanism of ΔE_C, we investigate ΔE_C^{-1} that follows a linear variation on a few hundred ps probe-delay range at all λ_p [we display the data corresponding to 550 nm pump wavelength Fig. 3(b)]. We already mentioned that solution of a nonlinear kinetic equation ($\frac{dN}{dt} = -k_2 N^2$) follows inverse-linear function $N(t) \sim N_0/(1 - k_2 N_0 t)$. This, again, suggests predominant bimolecular recombination originating from recombination of electron-hole that contribute to BGR. Therefore, the association of process 1 to BGR is correct. Moreover, we repeat the TA measurements on multilayered MoS_2 flakes on a quartz substrate and dispersed in a solvent (N, N Dimethylformamide) and compare the ΔE_C dynamics following 800 nm photoexcitation for both sample environments. While the redshift remains invariant up to a few nanosecond probe delay in the case of the substrate, it decays within first 1 ns for liquid solvent (see Fig. 10 of Ref. [23]). This is due to the fact that heat dissipation from the TMDC flakes to the surrounding solvent is much faster than the flakes exposed in air (thermal conductivity value $\sim$0.04 W m^{-1} K^{-1}) as DMF possess around five times higher thermal conductivity than air [53]. This observation is in line with the fact that the offset redshift effect at longer delays, related to process 2, is actually due to lattice heating. To further ascertain the attribution, we compare the estimated temperature rise from the excitonic peak shift from lattice heating with that of temperature increase from the total conversion of absorbed photon energy into thermal energy. At 500 nm photoexcitation $\Delta E_C|_{5 \text{ ns}} = 2.9 \pm 1$. Using a temperature-dependent shift of -0.45 meV/K [53], we estimate a $\Delta T = 6 \pm 2$ K rise of temperature for 500 nm pump with fluence 11.3 μJ/cm^2 (excitation density of 10^{19} per cm^3). Assuming total absorbed energy is converted to heat, we can estimate $\Delta T = \frac{\Delta E}{d \rho c_p}$ $= \frac{F(1 - 10^{-A})}{d \rho c_p}$, where F, A, d, ρ, and c_p are pump fluence, lin-

ear absorption coefficient at the pump wavelength, sample thickness, density, and specific heat capacity, respectively. Using $F = 11.3$ μJ/cm^2, $d = 30$ nm, $\rho = 5.06$ g cm^{-3}, and $c_p = 0.39$ J/gK [57], we get $\Delta T = 2$ K. Therefore, the experimentally observed ΔT is of same order to that expected from the absorption of the photon energy. This observation further bolsters our assignment of the offset ΔE_C to phonon-induced lattice heating. The appearance of the lattice heating effect (band gap renormalization) after the photoexcitation is dictated by the timescale of electron-phonon coupling processes (correlated electron-hole plasma formation). As discussed earlier, for 400 nm pump excitation, predominant $\sim$8 ps rise can be attributed to the EHP formation since the relative weight of BGR induced shift is significantly higher than the redshift due to lattice heating. In the following section we shall discuss more quantitatively and show with data fitting that the attributions of the rise times are correct, as the opposite assumption fails to fit the ΔE_C dynamics.

We sum up the exciton renormalization dynamics for varying pump wavelengths in a pseudocolor contour plot in Fig. 3(a). The ΔE_C values are normalized with respect to the maximum redshift $|\Delta E_C|$. In addition to the redshift dynamics, notably, for $\lambda_p \in (650, 800)$ nm, there is an initial blueshift that converts into a redshift within few ps. Similar results have been observed previously in A/B excitons in TMDCs, where it has been argued that exciton binding energy reduction dictates the blueshift [6]. We also attribute this to dynamic screening [37] induced exciton binding-energy reduction. Possibly, pump-induced mid-gap bound excitons introduce this screening that remains absent for higher pump-photon energies.

It is worthwhile to mention that the average absorption of a 30 nm thick flake is around unity [see Fig. 1(a)]. Hence, the bottom MoS_2 layer holds about ten times fewer excitations (carriers and excitons) than the topmost layer. There is a gradual change in the number of excitations per layer from top to bottom. As Lambert Beer's law is not valid here due to the multiple reflections and interference effects inside the thick flakes, it is pretty complex to find the exact number of excitations in each layer. Such effects might be relevant for light-matter interactions in any three-dimensional or quasi-three-dimensional crystals. As the AFM image displays, thicker layers are much less in number than 20–30 nm flakes. The share of optical response from thick flakes having a thickness in the range of 60 to 200 nm is less than 20% of the total optical response. In the present context, such nonuniformity may be relevant in two aspects: (a) intralayer diffusion and (b) nonuniform shift of the excitons in different layers. We have mentioned in Sec. S2.1 of Ref. [23] that intralayer heat diffusion is slow enough to be significant within a few ns time delay. Also, the intralayer carrier diffusion is ineffective since the diffusion coefficient is low, and the carriers recombine before the characteristic timescale. The other aspect is that a nonuniform excitonic shift in different layers of a flake might increase the inhomogeneous linewidth of the excitonic state following pump excitation. As we discussed, two factors introduce excitonic shift: band gap renormalization and lattice heating. Band gap renormalization is a quasistatic screening effect originating from the weakening of Coulomb potential due to the presence of charge carriers

in the environment. Multiple surrounding layers influence this environmental screening effect and hence, is expected to be nearly uniform in different layers. On the other hand, as the lattice temperature directly depends on the excess hot carrier density, nonuniform excitation density in different layers may introduce a slight variation in the lattice temperature. Yet, it is to be noted that like the pump pulse creates a nonuniform excitation, the probe measures more excitations residing in top layers than in the bottom layers, thereby inherently reducing the effect of inhomogeneous broadening stemming from nonuniform excitonic shift (in different layers) to some extent. The temporal evolution of the linewidth broadening ($\Delta\Gamma_C$) as depicted in Figs. 1(c) and 1(d) is much more complicated, as both the homogeneous and inhomogeneous broadening is involved. The homogeneous linewidth of the exciton predominantly increases due to pump-induced exciton-exciton, exciton-phonon, and exciton-carrier scattering events that eventually dephase the exciton faster [20,58] (see Ref. [23], Sec. S10).

We model the exciton renormalization dynamics considering contributions from EHP screening ($\Delta E_{EHP} \leqslant 0$), lattice heating ($\Delta E_{ph} \leqslant 0$), and a blueshift due to exciton binding-energy reduction ($\Delta E_{BE} \leqslant 0$) for $\lambda_p \geqslant 650$:

$$\frac{\Delta E_C(t)}{|\Delta E_C|_{max}} = [\Delta E_{EHP}(t) + \Delta E_{ph}(t) - m_{\lambda_p}\Delta E_{BE}(t)] * IRF,$$
$$m_{\lambda_p} = 0; \quad \lambda_p \in (400, 600 \text{ nm}),$$
$$m_{\lambda_p} = 1; \quad \lambda_p \in (650, 800 \text{ nm}), \tag{4}$$

where ΔE_{EHP} is estimated from solving a nonlinear differential equation, while the other two terms assume exponential dynamics:

$$\frac{d(\Delta E_{EHP})}{dt} = B_{EHP}k_{1,r}e^{-k_{1,r}t} - \left(\frac{k_2 N}{B_{EHP}}\right)\Delta E_{EHP}^2,$$
$$\Delta E_{ph} = B_{ph}(1 - e^{-k_{ph}t}), \quad \Delta E_{BE} = B_{BE}e^{-k_{BE}t}. \tag{5}$$

Here B_{EHP}, B_{ph}, and B_{BE} are fitting parameters suggesting relative strength of exciton resonance renormalization due to EHP, phonon, and exciton binding energy reduction. Also, k_{ph}, $k_{1,r}$, $k_2 N$, and k_{BE} are the fitting parameters that signify rate constants of carrier-phonon coupling, formation of EHP, electron-hole recombination (second-order) times initial carrier-density participating in EHP formation, and exciton binding-energy reduction, respectively.

The initial slow buildup of ΔE_C is dictated by the dominant band gap renormalization effect. To further ascertain, we consider that low carrier-phonon coupling rate k_{ph} (and not EHP formation rate $k_{1,r}$) describes the slow buildup of ΔE_C. Latter assumption yields a poor fit (see Ref. [23], Fig. 7) and proves the assumption false. Basically, the parameter $k_{1,r}$ describes the slow rise in the considered model. In Figs. 3(c) and 3(d) we present the fitted ΔE_C dynamics along with the individual contributions from the screening and lattice heating (and exciton blueshift) for two pump wavelengths. Similar results for the other pump wavelengths are shown in Fig. 8 of Ref. [23]. All fitting parameter values along with the variances are tabulated in Table 3 of Sec. S7 in Ref. [23]. We find that Eqs. (4) and (5) perfectly describe the temporal evolution of

exciton resonance renormalization. We present fitted k_{ph} values as a function of the pump wavelength in Fig. 3(e). These values, except that of the 400 nm pump, are in good agreement with recent studies [54,59]. From these data, $\sim 0.16 \pm 0.1$ ps electron-phonon scattering time (k_{ph}^{-1}) upon 400 nm photoexcitation might appear too fast. However, one important fact regarding the electron-phonon coupling is that it is dependent on the intra-/intervalley scattering processes. Precisely, the rate of phonon interactions depends on the momentum of the emitted (absorbed) phonons. It has been observed theoretically that phonon scattering rates increase (time reduces) at lower phonon momenta [59]. As the global conduction band minima in multilayered MoS$_2$ lies at Σ point, in the case of photoexcitation at K valleys, carriers subsequently relax to Σ valleys. In this process, mostly large momentum phonons are emitted (also absorbed). We note that the energy gap between the valence band and the conduction band in the Σ point is 2.98 eV [37]. The 400 nm (3.1 eV) photoexcitation directly populates the band edge at Σ point, which is also the global conduction band minima in multilayered MoS$_2$. Therefore, low-momentum phonons predominantly contribute to the lattice heating for 400 nm pump excitation. Possibly, this leads to the ultrafast electron-phonon scattering and lattice heating ($k_{ph}^{-1} \sim 0.16 \pm 0.1$ ps). However, at lower pump wavelengths, vertical transition at Σ direction is not possible. Instead, carriers at K direction are populated, which eventually relax to Σ valleys through intervalley scattering. The latter process involves multiple higher-momentum phonon emissions and occurs in (longer) ~ 1 ps timescale. Indeed, carrier-phonon coupling times below 0.5 ps have not been reported in the case of TMDCs [52]. It is worth noting that none of the reported studies has been performed with this particular pump excitation condition, that is, direct excitation of the conduction band global minima in multilayered TMDCs.

Notably, $k_{1,r} < k_{ph}$ for $\lambda_p \in (400 \text{ nm}, 650 \text{ nm})$ indicating EHP formation rate dictates the initial slow dynamics for these pump wavelengths. However, at higher pump wavelengths, both quantities are comparable since the carrier-phonon coupling rate decreases with a reduction in the carrier temperature (equivalently, excess photon energy). Notably, due to the coexisting redshift and blueshift dynamics at initial delays for $\lambda_p > 600$ nm, the obtained $k_{1,r}$, k_{ph}, and k_{BE} values display sizable upper and lower bounds indicating some uncertainties in these parameters could not be avoided.

Interestingly, the magnitude of second-order rate constant (k_2) times the initial carrier-density contributing to band gap renormalization (N) differs from $k_2 N_0$ (N_0 is the initial carrier-density participating in exciton bleaching), as derived from $\Delta A_C(t)$ by an average factor of $\sim 1/50$ [Fig. 3(f)]. While pump-induced free carriers lead to state-filling effects, they renormalize band gap upon electron-hole plasma formation. Careful investigation of the ratio N/N_0 at five different pump energies confirms that around 1%–3% photoinduced carriers introduce BGR as they form EHP. Pump wavelength-dependent values are tabulated in the fourth column of Table I. Surprisingly, this data reveal only a few percent of the injected free carriers form Coulomb-correlated electron-hole plasma that renormalize the quasiparticle band gap. A majority of the injected free carriers recombine (or form band edge excitons) without forming a plasma.

TABLE I. Electron-hole plasma formation threshold.

λ_p (nm)	t_D (ps)	Delay @ $\frac{2\pi}{\omega_{pl}} = \tau$ (ps)	$\frac{N}{N_0}$ (%)	$\frac{N(t_D)}{N_{max}}$ (%)[a]
400	4 ± 1	–	–	–
500	5 ± 1	–	–	–
550	8 ± 1	2.3 ± 0.3	2.5 ± 0.9	4
600	10 ± 1	1.9 ± 0.2	3.2 ± 0.6	1
650	9 ± 1	2.5 ± 0.3	1.6 ± 0.7	6
700	11 ± 1	1.9 ± 0.3	1.3 ± 0.5	3
750	10 ± 1	2.2 ± 0.3	4 ± 4	5

[a]These values have huge errors up to 80%–90% due to the very small values (same order as the noise level) of ΔA_C around t_D.

C. Transition from uncorrelated free carriers to coulomb-correlated electron-hole plasma

An intriguing property of the observed ΔE_C is the slow rise up to ~8 ps. Such slow exciton redshift dynamics have been observed earlier and been attributed to lattice heating [2]. However, in the present case, we have carefully isolated the timescales and relative amplitude of the lattice heating and BGR. For example, lattice heating time (k_{ph}^{-1}) for 400 nm pump wavelength is 0.1 ps [Fig. 3(e)], and as evident from Fig. 3(c), it has negligible relative amplitude as compared to the EHP induced BGR. We rule out phonon-induced heating effects and confirm that the slow rise ~8 ps originates from EHP screening. We identify this time as t_D. As mentioned in the previous section, the exact opposite assumption that slow rise is due to the lattice heating effect leads to poor fitting of the ΔE_C dynamics. Note that exciton binding energy reduction is observed for $\lambda_p \geqslant 650$ nm, and an initial blueshift is observed before t_D (see Ref. [23], Fig. 12 for additional discussions).

As discussed earlier, BGR is dictated by the electron-hole plasma via Coulomb screening and screened exchange interactions [Eq. (3)]. In multivalley semiconductors like TMDCs, BGR at a particular k point (quasimomentum) depends on the exchange effects of the carriers residing at the specific valence and conduction bands at the same k point [9]. The higher the population in each band, the higher is the exchange effect and the BGR. Moreover, intervalley exchange effects are negligible [9]. In our experimental scenario, the conduction or valence band of the BN region is instantaneously (i.e., within the IRF) populated by intervalley scattering irrespective of the pump-photon energy. Therefore, intervalley scattering does not affect the observed slow rise of the band gap renormalization. On the other hand, evolution of the screened Coulomb potential [$V_s(q)$] is subject to the formation of EHP that is known to be around inverse of plasma frequency ($\frac{2\pi}{\omega_{pl}} = \frac{2\pi}{\sqrt{\frac{Ne^2}{m^* \epsilon_0 \epsilon_r}}}$). Using plasma density (1/50 times injected carrier density), $N = \frac{1}{50} \times 10^{19}$ per cm^3, $\epsilon_r = 16$, $m^* = 0.525 m_0$, we estimate EHP formation time of 0.7 ps. This is an order lower than observed t_D and does not explain the underlying phenomenon for large t_D values.

To obtain further insight into the plasma formation, we compare the initial dynamics of ΔE_C following 415 nm photoexcitation at varying input carrier densities ranging from 3×10^{18} to 4×10^{19} per cm^3. We choose this particular pho-

ton energy as we observed a high k_{ph} value indicating fast carrier-photon coupling through lattice heating. This, in turn, helps easy distinction of the initial increase of BGR and lattice heating. We display ΔE_C up to 16 ps probe delay at five different carrier densities and mark t_D by yellow triangles (as a guide to the eye) in Fig. 4(c). For the lower carrier densities up to 1.1×10^{19} per cm^3, t_D reduce from 9 to 2 ps; however, jumps to 8 ps at input carrier density of 2×10^{19} per cm^3. Gradual reduction of t_D with increasing injected carrier density qualitatively follows the earlier prediction Ref. [16], as $\frac{1}{\omega_{pl}} \sim \frac{1}{\sqrt{N}}$ (see Ref. [23], Sec. S11 for further discussions).

Nonetheless, elevated t_D values at higher excitation densities remain unexplained. Briefly, the density-dependent slow rise of $|\Delta E_C|$ identifies a threshold of input carrier density beyond which plasma formation time cannot be correlated with the inverse of plasma frequency.

Afterward, we explore the electron-hole plasma formation criterion in context to this slow-rise dynamics of BGR. We recall that in order to form an electron-hole plasma, an essential criterion has to be satisfied [1,60]:

$$\omega_{pl}\tau \gg 1, \tag{6}$$

where τ is the dominant damping (scattering) time constant due to carrier-carrier, carrier-ion, or carrier-phonon interactions. This criterion reinforces that if the random collisions inside free-carrier gas are more frequent than the time period of the plasma wave, then the Coulomb correlation cannot form. According to the Drude model, the scattering time constant (τ) is inversely related to carrier density (N) as $\tau = \frac{m^*}{\rho N e^2}$, where ρ is resistivity. As the carrier concentration falls rapidly after photoexcitation, we need to check the validity of the relation (6) in the time domain to understand the plasma formation regime. We plot the delay-dependent instantaneous plasma oscillation period ($= \frac{2\pi}{\omega_{pl}}$) and scattering time constant (τ) considering the modeled carrier density dynamics (from the corresponding ΔA_C dynamics) for $\lambda_p = 600$ nm in Fig. 4(a). Resistivity is estimated from an earlier room-temperature transient absorption microscopy that finds carrier mobility of 170 ± 20 cm^2/V s of a bulk MoS$_2$ crystal [21] (see Ref. [23], Sec. S8 for details on the parameters). We observe that at initial delays, up to 1.9 ps, relation (6) remains invalid since τ is as small as 50 to 100 fs, whereas the plasma oscillation period is longer. Therefore, during this timescale, frequent carrier-scattering events (with other carriers, ions, or phonons) destroy the Coulomb correlation between charge carriers and a stable electron-hole plasma cannot form. However, at higher delays, as plasma oscillation period becomes sufficiently smaller than τ, EHP reaches a quasiequilibrium. We observe a maximum shift of the quasiparticle band gap at this quasiequilibrium around 8 ps when carrier scattering time is roughly four times the plasma oscillation period. An earlier pump-probe study suggests carrier-carrier scattering times ~10's of fs in few-layered MoS$_2$ at room temperature in the presence of excitation densities 10^{13}–10^{14} per cm^2 (areal excitation density used in our experiments is 0.25×10^{14} per cm^2) [52]. Therefore, we ascribe the slow buildup of EHP dynamics in MoS$_2$ to the huge damping due to ultrafast carrier-carrier scattering. In Fig. 4(b) we show a cartoon diagram of uncorrelated carriers and Coulomb-correlated EHP.
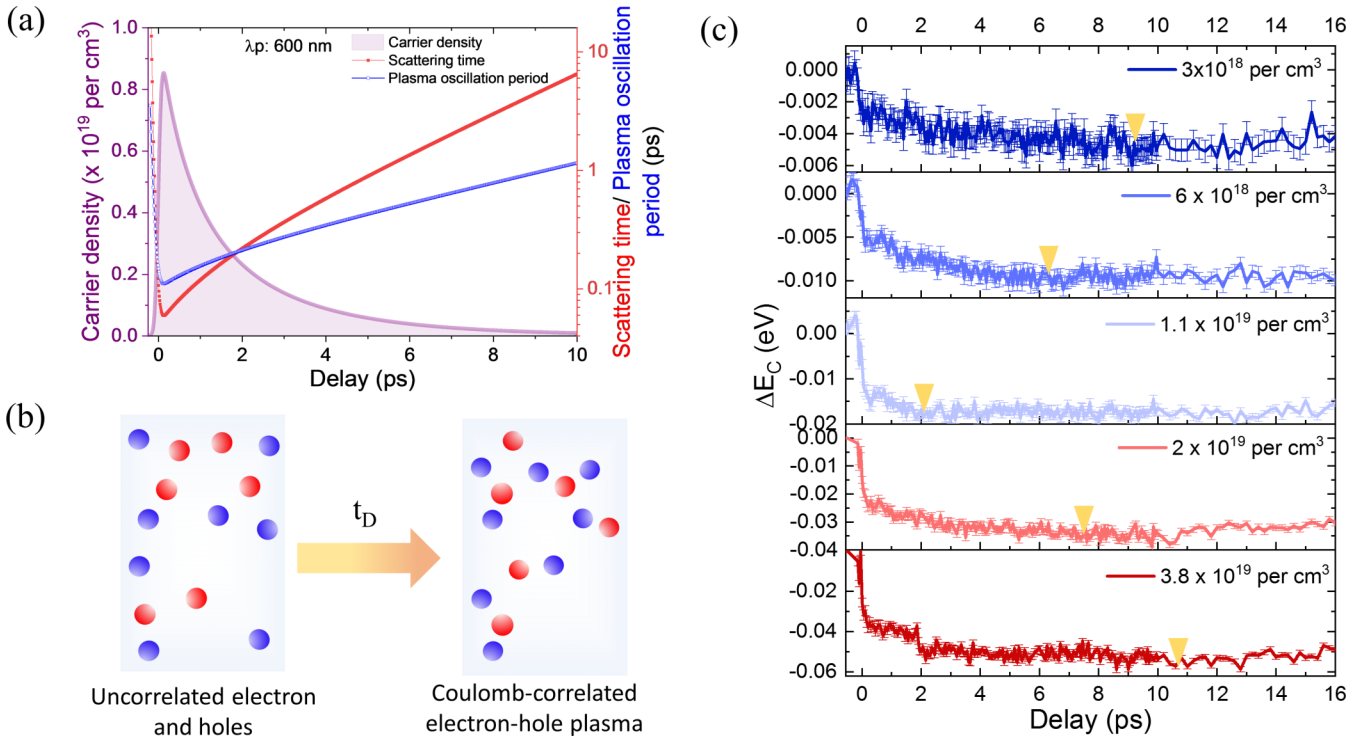
FIG. 4. (a) (axis: left) Variation of photoinduced carrier density, (axis: right) instantaneous scattering time (τ) and instantaneous plasma oscillation period ($\frac{2\pi}{\omega_{pl}}$) with probe delay. Here plasma oscillation period becomes less than the scattering time beyond a crossover probe delay of 1.9 ps. (b) Schematic representation of uncorrelated free-carrier gas and correlated electron-hole plasma. Red (blue) filled circles suggest holes (electrons). (c) Temporal evolution of ΔE_C upon 415 nm pump excitation with different excitation densities. A yellow triangle is inserted in each curve to indicate the probe delay at which $|\Delta E_C|$ reaches a maximum (t_D).

The transition from the former to the latter occurs at a ps timescale.

From the temporal dynamics of ΔE_C, we note t_D (time delay corresponding to the maximum value of $|\Delta E_C|$) and compare that with the probe delays corresponding to crossovers of τ and $\frac{2\pi}{\omega_{pl}}$ for each λ_p in Table I. Beyond the crossover point, the plasma oscillation period is less than the scattering time, and EHP formation is feasible when the former is sufficiently smaller than the latter ($\frac{2\pi}{\omega_{pl}} << \tau$). The crossover probe-delay values estimated by the Drude model suggests the retarded electron-hole plasma formation following the crossover delay. Roughly, t_D corresponds to $\frac{2\pi}{\omega_{pl}} \approx \frac{\tau}{4}$. As we depicted that carrier density falls drastically in ps timescale, this delay threshold for plasma formation further illuminates that fact—only 1%–3% of injected carrier form plasma and contribute to the band gap renormalization. We explore the ratio of carrier density at t_D and the maximum injected density (i.e., $\frac{N(t_D)}{N_{max}}$) from the ΔA_C dynamics. We compare that with the obtained ratio of EHP to injected carriers ($\frac{N}{N0}$) (see Table I). It turns out these values are in the same order and match decently for all pump wavelengths ranging from 550 to 750 nm. Note that ΔA_C dynamics for 400 and 500 nm photoexcitation is dictated by exciton dynamics, limiting us to perform such comparative demonstration.

In summary, we have observed the transition from a uncorrelated free-carrier gas to a Coulomb-correlated electron-hole plasma below the Mott density regime in a transition metal dichalcogenide through ultrafast optical spectroscopy. We look for distinguished signatures of uncorrelated electron-hole gas and correlated EHP in the photoinduced excitonic properties. We reveal that under high excitation density ($\sim10^{19}$ per cm^3), EHP formation is retarded up to 8 ps, and only 1%–3% photoexcited carriers contribute to the dressed EHP state. This initial retardation stems from huge damping due to carrier-carrier scattering. Such effect is negligible while the photoinjection density is lowered by one order ($\sim10^{18}$ per cm^3), which guarantees the plasma oscillation period is always smaller than the instantaneous damping time constant. This study presents an elemental understanding of the electron-hole plasma formation under high carrier injection. Importantly, we formulate a generalized time-resolved technique to isolate uncorrelated free carriers and Coulomb-correlated electron-hole plasma in excitonic semiconductors. As electron-hole plasma screening is a ubiquitous tool for tuning semiconductor device properties, this study opens up opportunities for effective optoelectronic device engineering.

[1] N. Ashcroft and N. Mermin, *Solid State Physics* (Saunders College, Philadelphia, 1976).

[2] E. J. Sie, A. Steinhoff, C. Gies, C. H. Lui, Q. Ma, M. Rsner, G. Schnhoff, F. Jahnke, T. O. Wehling, Y.-H. Lee, J. Kong, P. Jarillo-Herrero, and N. Gedik, Observation of exciton redshift-blueshift crossover in monolayer WS$_2$, Nano Lett. **17**, 4210 (2017).

[3] A. Chernikov, A. M. van der Zande, H. M. Hill, A. F. Rigosi, A. Velauthapillai, J. Hone, and T. F. Heinz, Electrical Tuning of Exciton Binding Energies in Monolayer WS$_2$, Phys. Rev. Lett. **115**, 126802 (2015).

[4] H. Haug and S. W. Koch, *Quantum Theory of the Optical and Electronic Properties of Semiconductors*, 5th ed. (World Scientific, Singapore, 2009).

[5] M. Stein, C. Lammers, M. J. Drexler, C. Fuchs, W. Stolz, and M. Koch, Enhanced Absorption by Linewidth Narrowing in Optically Excited Type-II Semiconductor Heterostructures, Phys. Rev. Lett. **121**, 017401 (2018).

[6] P. D. Cunningham, A. T. Hanbicki, K. M. McCreary, and B. T. Jonker, Photoinduced bandgap renormalization and exciton binding energy reduction in WS$_2$, ACS Nano **11**, 12601 (2017).

[7] N. P. S. W. K. A. Mysyrowicz, *Introduction to Semiconductor Optics* (Prentice Hall, Englewood Cliffs, NJ, 1993).

[8] P. Vashishta and R. K. Kalia, Universal behavior of exchange-correlation energy in electron-hole liquid, Phys. Rev. B **25**, 6492 (1982).

[9] H. Kalt and M. Rinker, Band-gap renormalization in semiconductors with multiple inequivalent valleys, Phys. Rev. B **45**, 1139 (1992).

[10] A. Steinhoff, M. Rsner, F. Jahnke, T. O. Wehling, and C. Gies, Influence of excited carriers on the optical and electronic properties of MoS$_2$, Nano Lett. **14**, 3743 (2014).

[11] K. F. Mak, K. L. McGill, J. Park, and P. L. McEuen, The valley Hall effect in MoS$_2$ transistors, Science **344**, 1489 (2014).

[12] Y. Ye, J. Xiao, H. Wang, Z. Ye, H. Zhu, M. Zhao, Y. Wang, J. Zhao, X. Yin, and X. Zhang, Electrical generation and control of the valley carriers in a monolayer transition metal dichalcogenide, Nat. Nanotechnol. **11**, 598 (2016).

[13] K. F. Mak, K. He, C. Lee, G. H. Lee, J. Hone, T. F. Heinz, and J. Shan, Tightly bound trions in monolayer MoS$_2$, Nat. Mater. **12**, 207 (2013).

[14] B. Lee, W. Liu, C. H. Naylor, J. Park, S. C. Malek, J. S. Berger, A. T. C. Johnson, and R. Agarwal, Electrical tuning of exciton-plasmon polariton coupling in monolayer MoS$_2$ integrated with plasmonic nanoantenna lattice, Nano Lett. **17**, 4541 (2017).

[15] D. Unuchek, A. Ciarrocchi, A. Avsar, K. Watanabe, T. Taniguchi, and A. Kis, Room-temperature electrical control of exciton flux in a van der Waals heterostructure, Nature (London) **560**, 340 (2018).

[16] R. Huber, F. Tauser, A. Brodschelm, M. Bichler, G. Abstreiter, and A. Leitenstorfer, How many-particle interactions develop after ultrafast excitation of an electron–hole plasma, Nature (London) **414**, 286 (2001).

[17] A. Steinhoff, M. Florian, M. Rösner, G. Schönhoff, T. O. Wehling, and F. Jahnke, Exciton fission in monolayer transition metal dichalcogenide semiconductors, Nat. Commun. **8**, 1166 (2017).

[18] E. A. A. Pogna, M. Marsili, D. De Fazio, S. Dal Conte, C. Manzoni, D. Sangalli, D. Yoon, A. Lombardo, A. C. Ferrari, A. Marini, G. Cerullo, and D. Prezzi, Photo-induced bandgap renormalization governs the ultrafast response of single-layer MoS$_2$, ACS Nano **10**, 1182 (2016).

[19] D. Sun, Y. Rao, G. A. Reider, G. Chen, Y. You, L. Brzin, A. R. Harutyunyan, and T. F. Heinz, Observation of rapid exciton-exciton annihilation in monolayer molybdenum disulfide, Nano Lett. **14**, 5625 (2014).

[20] C. Ruppert, A. Chernikov, H. M. Hill, A. F. Rigosi, and T. F. Heinz, The role of electronic and phononic excitation in the optical response of monolayer WS$_2$ after ultrafast excitation, Nano Lett. **17**, 644 (2017).

[21] N. Kumar, J. He, D. He, Y. Wang, and H. Zhao, Charge carrier dynamics in bulk MoS$_2$ crystal studied by transient absorption microscopy, J. Appl. Phys. **113**, 133702 (2013).

[22] S. Mukherjee, R. Maiti, A. Midya, S. Das, and S. K. Ray, Tunable direct bandgap optical transitions in MoS$_2$ nanocrystals for photonic devices, ACS Photonics **2**, 760 (2015).

[23] See Supplemental Material at http://link.aps.org/supplemental/10.1103/PhysRevB.104.075446 for additional discussion on sample characterization, experimental techniques, and data analysis.

[24] S. Srivastava and Y. N. Mohapatra, Determination of interlayer electron mobility in multilayer MoS$_2$ flake using impedance spectroscopy, J. Phys. D **54**, 295104 (2021).

[25] X. Zhang, D. Sun, Y. Li, G.-H. Lee, X. Cui, D. Chenet, Y. You, T. F. Heinz, and J. C. Hone, Measurement of lateral and interfacial thermal conductivity of single- and bilayer MoS$_2$ and MoSe$_2$ using refined optothermal raman technique, ACS Appl. Mater. Interfaces **7**, 25923 (2015).

[26] X. F. Yue, Y. Y. Wang, Y. Zhao, J. Jiang, K. Yu, Y. Liang, B. Zhong, S. T. Ren, R. X. Gao, and M. Q. Zou, Measurement of interfacial thermal conductance of few-layer MoS$_2$ supported on different substrates using raman spectroscopy, J. Appl. Phys. **127**, 104301 (2020).

[27] Y. Yu, T. Minhaj, L. Huang, Y. Yu, and L. Cao, In-plane and interfacial thermal conduction of two-dimensional transition-metal dichalcogenides, Phys. Rev. Appl. **13**, 034059 (2020).

[28] R. Wang, B. A. Ruzicka, N. Kumar, M. Z. Bellus, H.-Y. Chiu, and H. Zhao, Ultrafast and spatially resolved studies of charge carriers in atomically thin molybdenum disulfide, Phys. Rev. B **86**, 045406 (2012).

[29] L. Yuan, T. Wang, T. Zhu, M. Zhou, and L. Huang, Exciton dynamics, transport, and annihilation in atomically thin two-dimensional semiconductors, J. Phys. Chem. Lett. **8**, 3371 (2017).

[30] T. Yan, X. Qiao, X. Liu, P. Tan, and X. Zhang, Photoluminescence properties and exciton dynamics in monolayer WSe$_2$, Appl. Phys. Lett. **105**, 101901 (2014).

[31] L. A. Jauregui, A. Y. Joe, K. Pistunova, D. S. Wild, A. A. High, Y. Zhou, G. Scuri, K. De Greve, A. Sushko, C.-H. Yu, T. Taniguchi, K. Watanabe, D. J. Needleman, M. D. Lukin, H. Park, and P. Kim, Electrical control of interlayer exciton dynamics in atomically thin heterostructures, Science **366**, 870 (2019).

[32] W. Zheng, B. Zheng, Y. Jiang, C. Yan, S. Chen, Y. Liu, X. Sun, C. Zhu, Z. Qi, T. Yang, W. Huang, P. Fan, F. Jiang, X. Wang, X. Zhuang, D. Li, Z. Li, W. Xie, W. Ji, X. Wang *et al.*, Probing and manipulating carrier interlayer diffusion in van der Waals multilayer by constructing type-I heterostructure, Nano Lett. **19**, 7217 (2019).

[33] A. Raja, L. Waldecker, J. Zipfel, Y. Cho, S. Brem, J. D. Ziegler, M. Kulig, T. Taniguchi, K. Watanabe, E. Malic, T. F. Heinz, T. C. Berkelbach, and A. Chernikov, Dielectric disorder in two-dimensional materials, Nat. Nanotechnol. **14**, 832 (2019).

[34] S. Das, Y. Wang, Y. Dai, S. Li, and Z. Sun, Ultrafast transient sub-bandgap absorption of monolayer MoS_2, Light: Sci. Appl. **10**, 27 (2021).

[35] J. Zipfel, J. Holler, A. A. Mitioglu, M. V. Ballottin, P. Nagler, A. V. Stier, T. Taniguchi, K. Watanabe, S. A. Crooker, P. C. M. Christianen, T. Korn, and A. Chernikov, Spatial extent of the excited exciton states in WS_2 monolayers from diamagnetic shifts, Phys. Rev. B **98**, 075438 (2018).

[36] Y. Yu, Y. Yu, Y. Cai, W. Li, A. Gurarslan, H. Peelaers, D. E. Aspnes, C. G. Van de Walle, N. V. Nguyen, Y.-W. Zhang, and L. Cao, Exciton-dominated dielectric function of atomically thin MoS_2 films, Sci. Rep. **5**, 16996 (2015).

[37] M. Karmakar, S. Bhattacharya, S. Mukherjee, B. Ghosh, R. K. Chowdhury, A. Agarwal, S. K. Ray, D. Chanda, and P. K. Datta, Observation of dynamic screening in the excited exciton states in multilayered MoS_2, Phys. Rev. B **103**, 075437 (2021).

[38] K. Basu, H. Zhang, H. Zhao, S. Bhattacharya, F. Navarro-Pardo, P. K. Datta, L. Jin, S. Sun, F. Vetrone, and F. Rosei, Highly stable photoelectrochemical cells for hydrogen production using a SnO_2-TiO_2/quantum dot heterostructured photoanode, Nanoscale **10**, 15273 (2018).

[39] A. Ghosh, D. K. Chaudhary, A. Mandal, S. Prodhan, K. K. Chauhan, S. Vihari, G. Gupta, P. K. Datta, and S. Bhattacharyya, Core/shell nanocrystal tailored carrier dynamics in hysteresisless perovskite solar cells with ∼20% efficiency and long operational stability, J. Phys. Chem. Lett. **11**, 591 (2020).

[40] K. F. Mak, C. Lee, J. Hone, J. Shan, and T. F. Heinz, Atomically Thin MoS_2: A New Direct-Gap Semiconductor, Phys. Rev. Lett. **105**, 136805 (2010).

[41] A. Carvalho, R. M. Ribeiro, and A. H. Castro Neto, Band nesting and the optical response of two-dimensional semiconducting transition metal dichalcogenides, Phys. Rev. B **88**, 115205 (2013).

[42] A. Chernikov, C. Ruppert, H. M. Hill, A. F. Rigosi, and T. F. Heinz, Population inversion and giant bandgap renormalization in atomically thin WS_2 layers, Nat. Photonics **9**, 466 (2015).

[43] S. Schmitt-Rink, D. S. Chemla, and D. A. B. Miller, Theory of transient excitonic optical nonlinearities in semiconductor quantum-well structures, Phys. Rev. B **32**, 6601 (1985).

[44] F. Ceballos, Q. Cui, M. Z. Bellus, and H. Zhao, Exciton formation in monolayer transition metal dichalcogenides, Nanoscale **8**, 11681 (2016).

[45] L. Wang, Z. Wang, H.-Y. Wang, G. Grinblat, Y.-L. Huang, D. Wang, X.-H. Ye, X.-B. Li, Q. Bao, A.-S. Wee, S. A. Maier, Q.-D. Chen, M.-L. Zhong, C.-W. Qiu, and H.-B. Sun, Slow cooling and efficient extraction of c-exciton hot carriers in MoS_2 monolayer, Nat. Commun. **8**, 13906 (2017).

[46] P. Schiettecatte, P. Geiregat, and Z. Hens, Ultrafast carrier dynamics in few-layer colloidal molybdenum disulfide probed by broadband transient absorption spectroscopy, J. Phys. Chem. C **123**, 10571 (2019).

[47] P. Hein, A. Stange, K. Hanff, L. X. Yang, G. Rohde, K. Rossnagel, and M. Bauer, Momentum-resolved hot electron dynamics at the $2h-MoS_2$ surface, Phys. Rev. B **94**, 205406 (2016).

[48] R. Wallauer, J. Reimann, N. Armbrust, J. Gdde, and U. Hfer, Intervalley scattering in MoS_2 imaged by two-photon photoemission with a high-harmonic probe, Appl. Phys. Lett. **109**, 162102 (2016).

[49] R. Bertoni, C. W. Nicholson, L. Waldecker, H. Hübener, C. Monney, U. De Giovannini, M. Puppin, M. Hoesch, E. Springate, R. T. Chapman, C. Cacho, M. Wolf, A. Rubio, and R. Ernstorfer, Generation and Evolution of Spin-, Valley-, and Layer-Polarized Excited Carriers in Inversion-Symmetric WSe_2, Phys. Rev. Lett. **117**, 277201 (2016).

[50] R. Prasad, *Electronic Structure of Materials* (CRC, Boca Raton, FL, 2013).

[51] Y. Varshni, Temperature dependence of the energy gap in semiconductors, Physica **34**, 149 (1967).

[52] Z. Nie, R. Long, L. Sun, C.-C. Huang, J. Zhang, Q. Xiong, D. W. Hewak, Z. Shen, O. V. Prezhdo, and Z.-H. Loh, Ultrafast carrier thermalization and cooling dynamics in few-layer MoS_2, ACS Nano **8**, 10931 (2014).

[53] Z. Chi, H. Chen, Z. Chen, Q. Zhao, H. Chen, and Y.-X. Weng, Ultrafast energy dissipation via coupling with internal and external phonons in two-dimensional MoS_2, ACS Nano **12**, 8961 (2018).

[54] M.-F. Lin, V. Kochat, A. Krishnamoorthy, L. Bassman, C. Weninger, Q. Zheng, X. Zhang, A. Apte, C. S. Tiwary, X. Shen, R. Li, R. Kalia, P. Ajayan, A. Nakano, P. Vashishta, F. Shimojo, X. Wang, D. M. Fritz, and U. Bergmann, Ultrafast non-radiative dynamics of atomically thin $MoSe_2$, Nat. Commun. **8**, 1745 (2017).

[55] M. M. Glazov and A. Chernikov, Breakdown of the static approximation for free carrier screening of excitons in monolayer semiconductors, Phys. Status Solidi B **255**, 1800216 (2018).

[56] A. Steinhoff, M. Florian, and F. Jahnke, Dynamical screening effects of substrate phonons on two-dimensional excitons, Phys. Rev. B **101**, 045411 (2020).

[57] L. S. Volovik, V. V. Fesenko, A. S. Bolgar, S. V. Drozdova, L. A. Klochkov, and V. F. Primachenko, Enthalpy and heat capacity of molybdenum disulfide, Sov. Powder Metal. Met. Ceram. **17**, 697 (1978).

[58] G. Moody, C. Kavir Dass, K. Hao, C.-H. Chen, L.-J. Li, A. Singh, K. Tran, G. Clark, X. Xu, G. Berghäuser, E. Malic, A. Knorr, and X. Li, Intrinsic homogeneous linewidth and broadening mechanisms of excitons in monolayer transition metal dichalcogenides, Nat. Commun. **6**, 8315 (2015).

[59] L. Waldecker, R. Bertoni, H. Hübener, T. Brumme, T. Vasileiadis, D. Zahn, A. Rubio, and R. Ernstorfer, Momentum-Resolved View of Electron-Phonon Coupling in Multilayer WSe_2, Phys. Rev. Lett. **119**, 036803 (2017).

[60] F. F. Chen, *Introduction to Plasma Physics and Controlled Fusion* (Springer, Berlin, 2016).